Journal Pre-proofs

Silver (Ag) doped graphitic carbon nitride (g-C_3N_4)/biochar composite photocatalyst for improved photocatalytic degradation of ciprofloxacin (CIP)

Ijlal Idrees, Muhammad Zafar, Malik Adeel Umer, Fahad Rehman, Abdul Razzaq, Seongwan Kim, Yunsook Yang, Woo Young Kim

PII: S2211-3797(24)00756-3
DOI: https://doi.org/10.1016/j.rinp.2024.108071
Reference: RINP 108071

To appear in: *Results in Physics*

Received Date: 7 October 2024
Revised Date: 25 November 2024
Accepted Date: 4 December 2024

Please cite this article as: Idrees, I., Zafar, M., Umer, M.A., Rehman, F., Razzaq, A., Kim, S., Yang, Y., Kim, W.Y., Silver (Ag) doped graphitic carbon nitride (g-C_3N_4)/biochar composite photocatalyst for improved photocatalytic degradation of ciprofloxacin (CIP), *Results in Physics* (2024), doi: https://doi.org/10.1016/j.rinp.2024.108071

Silver (Ag) Doped Graphitic Carbon Nitride (g-C_3N_4)/Biochar composite Photocatalyst for Improved Photocatalytic Degradation of Ciprofloxacin (CIP)

Ijlal Idrees[1,†], Muhammad Zafar[2,†], Malik Adeel Umer[3], Fahad Rehman[1], Abdul Razzaq[1,*], Seongwan Kim[4], Yunsook Yang[4], Woo Young Kim[4,*]

[1] Department of Chemical Engineering, COMSATS University Islamabad, Lahore 54000, Pakistan

[2] Institute of Energy and Environmental Engineering, University of the Punjab, Lahore 54590, Pakistan

[3] School of Chemical and Materials Engineering (SCME), National University of Sciences and Technology (NUST), H-12, Islamabad 44000, Pakistan

[4] Department of Electronic Engineering, Faculty of Applied Energy System, Jeju National University, Jeju-si 63243, Jeju Special Self-Governing Province, Korea

[*] Authors to whom correspondence should be addressed.

[†] These authors contributed equally to this work.

Abstract

Dumping pharmaceutical wastewater into aquatic bodies vigorously adds to environmental pollution and amplifies antibiotic-resilient bacteria (ARB), a potential danger to humans and living organisms. Among several wastewater treatment methods, the photocatalysis approach under the umbrella of advanced oxidation processes (AOPs) offers sustainable, inexpensive, and comprehensive treatment of emerging pharmaceutical pollutants (PEPs). Until today, amongst a variety of photocatalysts developed, graphitic carbon nitride, g-C_3N_4, (GCN), is considered a relatively low-cost, harmless, thermally stable, and to some extent visible light active (VLA) photocatalyst. Further, Biochar (BC) has emerged as an environmentally friendly carbonaceous compound with good surface area, adsorption, and electrical conductivity. Hence being inspired by the characteristics of GCN and BC, a facile and captivating approach of composite photocatalysts comprising ternary components Ag, GCN, and BC is executed in the present work. The pivotal focal point is to enhance the optical absorption of GCN photocatalyst within visible light range by silver (Ag) doping strategy and boost the photogenerated charges separation by coupling with BC, both factors ultimately upsurging the photocatalytic performance. The photocatalytic performance of synthesized Ag-doped GCN/Biochar (ABCN) composite photocatalysts is assessed via the degradation of Ciprofloxacin (CIP) antibiotic, a common quinolone. The photocatalytic performance is optimized by varying the content of Ag dopant in the composite photocatalyst. The best sample 0.10-ABCN (with 10 wt.% Ag content) exhibits the highest photocatalytic activity i.e. 70 % degradation of CIP (after 4 h of light irradiation), which is 3 times better than the pure GCN sample (25 %). Results from experimentation suggest that the strategy of composite photocatalyst fabrication based on the doping effect and fusing with carbonaceous material improved the photocatalytic efficiency mainly ascribed to improved optical absorbance and efficient charge separation.

Keywords: Composite photocatalyst, Ag Doping, Biochar, Graphitic carbon nitride (GCN), Ciprofloxacin (CIP) antibiotic, Photocatalytic degradation

1. Introduction

Due to the increased urbanization and industrialization, the pollution problem has become more severe with water pollution, the most important having wide scale impact as it is the only natural resource present in abundance and is used by every living being [1]. A lot of industries have been reported that are causing water pollution including mining operations, manufacturing processes, and chemical plants. These industries are causing noticeable damage to human health and aquatic life by releasing effluents that are rich in suspended solids, heavy metals, and organic compounds. The pharmaceutical industry among the industries is the most hazardous as it releases active pharmaceutical ingredients (API), personal care products, and metabolites collectively known as micropollutants in water bodies. These micropollutants due to their persistent and bioactive nature are not completely removed through conventional wastewater treatment technique [2]. That is why pharmaceutical micropollutants are considered severe and extensive modern issues, not only polluting the water but also leading to disruption of ecological cycles. Water bodies polluted by antibiotics, a significant pharmaceutical micropollutant, are of utmost importance as it has affected a large scale of the population, especially during COVID-19 [3]. These antibiotics are also the main reason for the breeding of antibiotic-resilient bacteria (ARB) by abolishing already present bacterial colonies in the ecosystem and destroying their natural competition ultimately enhancing their ability to resist antimicrobial activity [4]. Among certain antibiotics, Ciprofloxacin (CIP) is the most used antibiotic in human and livestock breeding for the sake of disease prevention. CIP is difficult to remove by traditional removal methods and is also naturally hydrophobic, which allows it to form agglomeration in wastewater streams, making its treatment a bit challenging. Conventional degradation of CIP with time is also causing secondary pollution by releasing toxic intermediate products[5]. Therefore, a need has arisen to remove CIP in a cost-effective and environmentally friendly way.

Effluent treatment for the removal of pollutants involves a variety of treatment methods biological, physical, and chemical. Microorganisms are used in biological treatment to remove pollutants from effluent streams while coagulation, flocculation, and disinfection fall in the category of chemical wastewater treatment whereas, physical wastewater treatment includes sedimentation, screening, and filtration for the removal of solid particles. Some other methods also fall in the category of advanced wastewater treatment and include ion exchange, advanced oxidation process (AOP), and membrane filtration. These methods are used to keep a strict eye on effluent quality in advanced industries and are very helpful in dealing with micropollutant issues. On the other hand, combining these techniques or using them separately will only contribute to the efficiency of industrial wastewater treatment processes resultantly improving the water quality and environmental cleanliness [6–8]. Among various treatment technologies, photocatalysis under the domain of AOP is considered a simple technique that gained prominence after the work of Fujishima and Honda where they produced hydrogen (H_2) from water under solar light irradiation of TiO_2 [9]. Photocatalysis, with its exceptional tendency of application in different environmental and energy-related scenarios, is the most effective in wastewater treatment procedures. A variety of applications like energy production, organic synthesis, and environmental remediation also involve semiconductor materials like TiO_2, SnO_2, ZnO, Fe_2O_3, $BiVO_4$, etc. [10–16]. Individually, these photocatalysts have their qualities and shortcomings. Some of these photocatalysts show limited light absorption in the visible region and absorb only ultraviolet (UV) radiation. This not only limits their photocatalytic efficiency but also skips a large portion of visible light that is already available in sunlight to harness. The photocatalytic process is also seriously affected by the rapid

recombination of electrons and holes. Therefore, it is also prudent to improve the separation of electrons and holes for higher photocatalytic efficiencies using various modification techniques [17,18].

Currently, the most outstanding polymeric photocatalyst is graphitic carbon nitride, g-C_3N_4 (GCN). Its visible light active band gap of 2.7eV and appropriate positions of the conduction band (CB) and valance band (VB) are very suitable for photocatalytic applications. This material not only transforms organic and inorganic contaminants into innocuous byproducts but also converts CO_2 into energy-abundant complexes. The chemical and thermal stability of GCN is high enough to safeguard it under severe circumstances of high temperature and reactive chemical atmosphere. Still, this polymeric photocatalyst like other photocatalysts has some shortcomings of low surface area and quick electron-hole recombination. Many studies emphasize the need for a GCN-based environmentally and economically favorable photocatalyst for the removal of antibiotics [19]. Therefore, it is compulsory to further alter GCN with economic dopants and composite materials to enhance its photocatalytic properties and make it an economically viable photocatalyst [20]. To improve its optical absorption and photogenerated charges separation and visible light absorption, different strategies are suggested that include molecular and elemental doping [21,22], exfoliation of GCN [23], preparation of mesoporous GCN [24], nanocomposite formation with other semiconductors [25] and dye sensitization [26]. It is well established that GCN has a tunable band gap with manageable highest occupied molecular orbital (HOMO) and lowest unoccupied molecular orbital (LUMO). Therefore, it can greatly affect the photocatalytic performance of GCN as a functional polymeric photocatalyst. The tunable band gap of GCN makes the modification process easy largely by element doping. Knowingly, doping, which is intended by purposely adding impurities, is recognized to be an effective technique to tune the band gap of GCN, which significantly modifies the band gap favoring visible light absorption and effective electron-hole pairs separation [27]. The chemical framework of photocatalysts is extensively altered through noble metals which improve the light-absorption range and extend the lifetime of photogenerated charges (electron-hole pair). For instance, noble metals such as Au and Ag, exhibit certain surface plasmon resonances which results in resonance peaks in the visible-light region [28]. Therefore, noble metals are good electron acceptors that improve visible-light absorption of the photocatalyst and resultantly the number of photogenerated charges. More significantly, noble metals enhance the separation of these charges produced by light [29].

Photogenerated charges recombination, particularly for GCN, is another challenge limiting photocatalytic performance. To improve the photogenerated charge separation surface, coupling with carbonaceous materials possessing good capacity to extract the photogenerated charges offers a sustainable and eco-friendly solution. Among carbonaceous materials, biochar has attracted researcher's attention because of a green substitute for other materials that are chemically synthesized and it can be simply prepared from renewable and adequately plentiful resources [30]. As a natural carbonaceous resource, biochar (BC) enhances photogenerated charge separation and provides a conductive pathway to reaction sites [31]. Due to its immense benefits, BC is considered to be the most suitable and sustainable compound to be used for the removal of pharmaceutical micropollutants like antibiotics and antibiotic-resistant genes from aqueous mediums in an eco-friendly manner [32].

Until today, many studies have been conducted where composite photocatalyst formation along with elemental surface modification are combined to assess the favorable outcomes of

photocatalytic wastewater treatment. For instance, the development of co-modified nitrogen-doped GCN loaded with CeO_2 (CeNCN) showed an extended visible light absorbance and effective photogenerated charge separation. CeNCN showed outstanding degradation efficiency with a tetracycline removal rate of 80.09 % in 60 min. [33]. In another study, photocatalytic degradation of 98.75% of malachite green (MG) dye was achieved by employing manganese oxide doped graphene oxide/zinc oxide (GO-ZnO/Mn_2O_3) ternary composite. The key performance parameters were an increased surface area of 75.35 m^2/g and a narrowed bandgap of 1.6 eV [34]. In another research work, visible light-active carbon-doped TiO_2 supported by metal nitrate hydroxide (CT-Ni/Co/Cu) nanocomposite was studied for the degradation of tetracycline. In this study, 98% of tetracycline was reported to be removed after 60 min. of light irradiation [35]. Similarly, a new BiOCl/Cu-doped Bi_2S_3 photocatalyst was considered to capably remove CIP with high photocatalytic activity. The photocatalytic degradation rate of CIP was reported to be 97.1% at 20 mg/L concentration with 20 min of visible light treatment [36]. In a recent study, Ni-doped α-Fe_2O_3/g-C_3N_4 (NFGCN) photocatalysts were produced through a facile co-precipitation method and used for the degradation of CIP and methylene blue (MB) via photocatalysis. The as-prepared photocatalyst exhibited remarkable photocatalytic activity with decent degradation efficiency of 82.1 % and 92.0 % for CIP and MB, respectively, within 120 min. of sunlight exposure [22]. Similarly, there are a lot of other ternary composites reported in the literature that exhibit excellent degradation properties for antibiotics [37–39].

Being inspired by the alluring benefits and advantages of composite photocatalyst employing a ternary materials concept, the present research work exhibits the development of a composite photocatalyst comprising of Ag-doped GCN photocatalyst coupled with biochar (BC), a rich carbonaceous and electron conductive entity. Ag-doped GCN/Biochar composite photocatalysts were prepared by a facile two-step synthesis approach: (i) In the first step Ag doped GCN precursor is prepared with varied content of Ag dopant and Urea (GCN precursor), which is then (ii) mixed with a fixed quantity of biochar and subjected to thermal polycondensation for the synthesis of Ag-doped GCN/Biochar composite photocatalyst. It is expected that at one end Ag dopant will improve the light absorption of GCN in the visible range due to the narrowing of the bandgap whereas on the other end biochar network in the composite photocatalyst will promote the photoexcited charges separation and mobility. Hence both parameters will lead to a significant uplift in the photocatalytic performance of the resultant ternary material-based composite photocatalyst. It is expected the outcomes of the present research work will provide engaging and tempting ways to design photocatalyst architecture with enhanced photocatalytic performance.

Experimental

2.1. Chemicals and consumables

Urea ($NH_2CONH_2 \geq 98.9\%$) was purchased from PENTA CHEMICALS PVT. LTD. and was employed for the synthesis of pure GCN and composite photocatalysts. As a dopant, silver nitrate ($AgNO_3$, ACS grade $\geq 98.9\%$) from VWR CHEMICALS was used. BC was synthesized by the pyrolysis method using waste eggshells. Both chemicals were used as receieved without any changes and BC was prepared locally in the lab. Deionized water (DI) was utilized as a solvent for washing and mixing and obtained from Aqua Flow reverse osmosis water purifier system, made in Taiwan. Ciprofloxacin (CIP) antibiotic was a key pharmaceutical micropollutant investigated in the present study and used to gauge the photocatalytic activity of the prepared composite photocatalysts. This antibiotic was obtained from Pakheim International Pharmaceuticals PVT. LTD, Pakistan.

2.2. Preparation of pure graphitic carbon nitride (pure GCN)

A common thermal polycondensation procedure was used for the synthesis of pure graphitic carbon nitride (GCN). Mortar and pestle were used to crush 20 g of urea which was taken in a 100 ml crucible. This crushed urea was then treated in a muffle furnace at atmospheric conditions (550°C for 3 h). After natural cooling, the crucible containing pale yellow powder was taken out from the muffle furnace and crushed using mortar and pestle. This powder was then washed thoroughly using DI water and filtered using a vacuum filtration assembly. The obtained filtered wet cake was dried at 75 °C overnight. The final product was labeled as pure graphitic carbon nitride (GCN) [40–43].

2.3. Preparation of Biochar (BC)

BC was prepared by pyrolysis technique as reported [44]. The eggshells were collected and appropriately washed with DI water. Then these eggshells were dried in a drying oven at a temperature of 105 ℃ for 24 hours. The dehydrated eggshells after drying were crushed to fine white powder which was again exposed to drying in oven at 105 ℃ (overnight) for removal of any remaining moisture content. The dried and grounded eggshells were subjected to pyrolysis in a muffle furnace for 2 h at 500 ℃. After the treatment in a muffle furnace, a black residue product was naturally cooled, crushed, thoroughly washed, and dried. The concluding dried product, i.e. BC is collected in a glass vial and was used for the preparation of composite photocatalyst.

2.4. Preparation of Ag-doped GCN/BC (*x*-ABCN) composite photocatalyst

The synthesis process of composite photocatalysts followed a similar method as that of pure GCN with minor alterations. Different concentrations of silver nitrate ($AgNO_3$) were added to a glass beaker with 50 ml DI water having 10 g urea and stirred for half 30 min. on a hot plate stirrer. A milky mixture was obtained after mixing which was vaporized on the same hot plate stirrer at 75 °C under incessant stirring. The resultant semicrystalline liquid that solidified upon cooling was

ground to a fine powder using mortar and pestle. After crushing, the obtained powder was mixed with a specified amount of BC for 10 min. using mortar and pestle. This mixture of $AgNO_3$, Urea, and BC, was then subjected to a muffle furnace in a ceramic crucible for a thermal polycondensation process at 550 °C for 3h (like pure GCN), followed by natural cooling, crushing, washing, vacuum filtration and finally drying (at 75 °C overnight). A variety of composite photocatalysts were synthesized by varying the Ag dopant concentration i.e. $AgNO_3$ and are termed as *x*-ABCN where *x* represents the amount of silver nitrate ($AgNO_3$) added into the mixture i.e.0.05g, 0.07g, 0.10g, 0.13g, and 0.15g.

2.4. Characterization of prepared material

PANalytical X-pert Pro DY38059 Powder diffractometer, using 0.154 nm Cu Kα radiations was employed to study the crystalline structure of the prepared composites. Fourier transform infrared spectroscopy (THERMO NICOLET 6700 USA) was used to study the existence of organic and inorganic compounds by identifying their functional groups. Photoluminescence spectra (PL) with a laser excitation source of 457 nm (model: RENISHAW's InVia Raman Microscope UK) assessed the recombination of photoexcited charges. Scanning electron microscope (SEM) model JSM-6490A was used to obtain SEM images of the samples and study the surface morphology of prepared composite photocatalysts. Jasco V-770 UV-visible/Near Infrared spectrophotometer furnished with an integrating sphere was used to study the light absorbance of the prepared composites through UV-VIS DRS spectra.

To estimate the band gaps (Eg) of the synthesized composite photocatalysts, Tauc's relation was used which is given below [45]:

$$(\alpha h\nu)^{n} = A(h\nu - Eg) \qquad \text{Eq. 1}$$

Here, photon energy is denoted by hν where h is Planck's constant and ν is the frequency of light, the molar absorption coefficient is represented by α, the number of transitions by n, Tauc's constant by A, and the normal band gap of respective material by Eg.

2.5. Photocatalytic performance evaluation

The photocatalytic responsiveness of the prepared composite photocatalysts was gauged by their visible light-assisted degradation of antibiotic CIP targeted as a pharmaceutical micropollutant. The samples employed for assessment of photocatalytic activity include pure GCN, and composite photocatalysts, *x*-ABCN (where *x* represents the amount of Ag dopant) i.e. 0.05-ABCN, 0.07-ABCN, 0.10-ABCN, 0.13-ABCN and 0.15-ABCN. 100 ml of 50 ppm CIP solution was prepared in DI water and added to the photocatalytic reactor, followed by the addition of 50 mg of the photocatalyst sample, and the resulting suspension was stirred for 1 h under dark condition to achieve adsorption-desorption symmetry. The CIP liquid sample was taken from the photocatalytic reactor after dark time and centrifuged (at 5000 rpm for 5 min.) to separate the photocatalyst powder and CIP liquid. The clear CIP liquid was then transferred to a quartz cuvette and placed in a UV-VIS spectrophotometer where its absorption spectrum was attained. After dark, the photocatalytic reactor was irradiated by 5W LED light, and sampling was done from the reactor for every 15 minutes of the reaction according to a procedure like dark conditions. The overall photocatalytic performance evaluation experiment comprised of 4 h of light irradiation. The degradation results of CIP for 0.05-ABCN, 0.07-ABCN, 0.10-ABCN, 0.13-ABCN, and 0.15-ABCN were obtained using the above-mentioned procedure. The efficiency of CIP degradation in terms of its concentration every 15 min. was calculated using the following relation [46] :

$$\text{Rate of degradation} = \frac{C_* - C_T}{C_*} \times 100 \qquad \text{Eq. 2}$$

Where C_T is the concentration of CIP every 15 min.

C_* is referred to as the initial and fixed concentration of CIP

The pseudo-first-order kinetic model was considered for the calculation of the reaction rate for the degradation of CIP. The rate equation for the pseudo 1st order kinetic model is given below [47] :

$$kt = \ln\left(\frac{C_t}{C_*}\right) \qquad \text{Eq. 3}$$

3. Results and discussion

3.1 X-ray Diffraction (XRD) analysis (XRD)

X-ray diffraction analysis (XRD) patterns obtained for crystallinity analysis are shown in Fig.1. As BC is synthesized using eggshells, which are composted with pure GCN to produce composites, many diverse kinds of minerals and materials are observed in XRD patterns. Fig. 1a shows the XRD pattern for pure BC, Fig. 1b for pure GCN, and Fig. 1(c-g) exhibits XRD patterns of *x*-ABCN composite photocatalyst samples. It is observed that pure BC shows a peak corresponding to Ca $(OH)_2$ at $2\theta = 18.08^{\circ}$, whereas for all *x*-ABCN composite photocatalyst samples similar peak

appear around 2θ value of 20.89°. Further, XRD peaks appearing at 2θ = 21.08° to 65.08° for pure BC, 2θ = 22.3° to 60.2° for 0.05-ABCN, 2θ = 21.12° to 65° for 0.07-ABCN, 2θ = 22.16° to 64.78° for 0.10-ABCN, 2θ = 21.02° to 64.78° for 0.13-ABCN and 2θ = 21.16° to 60.24° for 0.15-ABCN depicts the existence of $CaCO_3$ in the edifice of BC and all *x*-ABCN composite photocatalysts. It can also be noticed that the occurrence of $Ca(OH)_2$ peak is quite apparent in BC, 0.05-ABCN, 0.07-ABCN, and 0.10-ABCN samples, whereas becomes less intense in 0.13-ABCN and 0.15-ABCN samples which signifies the fact that with increase in concentration of Ag dopant, Ca $(OH)_2$ and $AgNO_3$ reacting and generating silver oxide (Ag_2O) and calcium nitrate (Ca $(NO_3)_2$) [48]. The peaks appearing at 38° can be associated with silver oxide (Ag_2O), whereas Ca $(NO_3)_2$ can be assumed to render calcium (Ca^{2+}) and nitrate ($2NO_3^-$) ions as reported in the literature [49]. Dolomite ($CaMg(CO_3)_2$) and Dolomite combined with calcite ($CaCO_3$) can be characterized by peaks appearing around 2θ = 68°, 77° and around 2θ = 70°, 73°, 76°, for BC and all *x*-ABCN composite photocatalyst samples, respectively. It is also a good point to state here that the occurrence of calcium (Ca) and magnesium (Mg) components in BC and *x*-ABCN composite photocatalyst samples favors the successful synthesis of BC using eggshells and its use in composite synthesis [50,51]. For the BC sample, a crystalline carbon plane (002), is vibrant from the peaks located at 26.88° and 43.44° displaying the graphitic constitution of BC [52]. However, minor peaks around 43° appearing in *x*-ABCN samples indicate effective doping of Ag in the GCN framework combined with BC [53–58]. The successful synthesis of pure GCN is well justified by the pure GCN XRD pattern of pure GCN sample showing the distinctive peaks appearing around 2θ values of 13° and 27°, ascribed to characteristics planes of (100) and (002) of GCN organized by C-N groups. Similar peaks are also observed for all *x*-ABCN composite photocatalyst samples well establishing the composite containing GCN content[59–64]. Moreover, in all *x*-ABCN samples, the distinctive GCN peak (around 27°) is joined by small peaks or embedded in the main distinctive peak of GCN. This can be attributed to the reason that the graphitized structure of BC is immersed in the structure of GCN [65]. Therefore, peaks appearing around 29° and 60° can be ascribed to the (200) and (211) planes of graphite which further approves the effective insertion of BC in GCN structure [66]. Additionally, peaks appearing around 39°, 55°, 57°, and 68° are distinctive peaks for CaO, whereas peaks for Ca $(OH)_2$ are revealed around 47°, 48° and 50°. As silver (Ag) confirmed the availability of defect states in the photocatalytic material, CaO and $Ca(OH)_2$ can offer active sites for pollutant (CIP) capturing. Conferring to familiar reports, CaO was prepared by the calcination of $CaCO_3$ during the thermal polycondensation process, whereas Ca $(OH)_2$ was prepared naturally by the reaction of produced CaO with water in the sample and atmosphere [67].

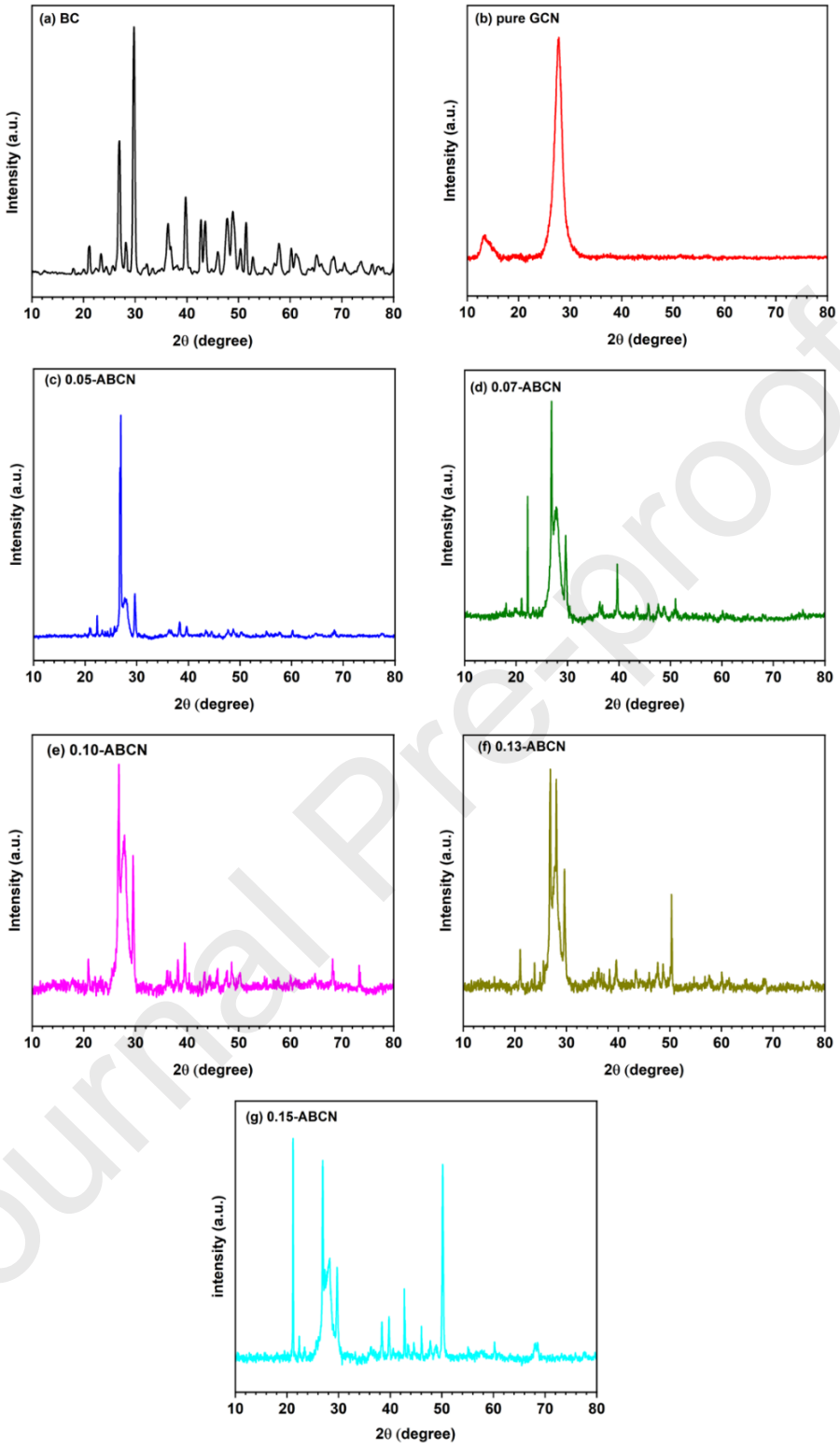

Figure 1. XRD patterns of (a) biochar (BC), (b) pure GCN, and (c-g) *x*-ABCN composite photocatalyst samples (where *x* = 0.05g, 0.07g, 0.10g, 0.13g, and 0.15g of $AgNO_3$).

3.2. Fourier transform infrared spectroscopy (FTIR)

Fig. 2 shows FTIR spectra of BC, pure GCN, and *x*-ABCN samples. For pure GCN (Fig. 2b), the peak around 3170 cm^{-1} is stronger as compared to BC (Fig. 2a) which indicates the C-H and N-H stretching vibrations. The bands observed at 1635 cm^{-1}, 1548 cm^{-1}, 1396 cm^{-1}, 1320 cm^{-1} and 1226 cm^{-1} display stretching vibrations mode of C-N heterocycles [68,69]. Similarly, the bands or patterns at 1135 cm^{-1} and 1064 cm^{-1} indicate C-O and C-C=O bonds in pure GCN structure indicating possible impurities [70]. The warping mode of N-H is represented by a peak at 883 cm^{-1}. Triazine and heptazine ring's intense bending vibrations are shown at 810 cm^{-1} representing the characteristic pattern of g-C_3N_4 and displaying the tri-s-triazine structure of pure GCN [71,72].

On the other hand, all samples show a comprehensive band within wavenumber 2900-3900 cm^{-1}, which can be ascribed to surface O-H, N-H, and C-H elongating vibrations. These patterns or peaks within 3600-3920 cm^{-1} are found to be increasing or decreasing in intensity indicating the functionalization of the OH group and the creation of O-H bonds independently or with other elements present in composite samples. However, for the BC sample, this band within 3600-3920 cm^{-1} exhibits a moderate puny peak at 3639 cm^{-1} which is ascribed to O-H group concentration in BC at the edges [73–77]. Broad and suppressed peaks appearing between 2300 to 2410 cm^{-1} in BC, 0.05-ABCN, 0.07-ABCN, 0.10-ABCN, 0.13-ABCN, and 0.15-ABCN can be ascribed to the presence of S-H extending vibrations of sulfhydryl groups found in the amino acid remains of collagen present in eggshell, representing the incorporation of BC structure in composite matrix [78,79]. Similarly, in the BC sample, the patterns at 2171 cm^{-1} and 1982 cm^{-1} show various manners of C≡C vibrations and allene C═C═C stretching vibrations [80,81]. Peaks appearing between 2131-2252 cm^{-1} in composite samples show the formation of the cyano group due to the addition of Ag particles and cause the tri-s-triazine unit to break replacing the C-N bond with C≡N, which proves the successful doping of Ag particles [28,82]. Furthermore, in BC and composite samples, the band appearing within the range of 1403-1648 cm^{-1} represents vibrations of conjugated C═C group and C-H vibrations of -CH_3 and -CH_2 groups [83]. Peaks observed within the range of 1333-1069 cm^{-1} for composite photocatalyst samples display C-O-C extending vibrations and C-N vibrations of the carbon nitride heterocyclic structure showing the effective synthesis of BC and incorporation of BC in GCN-based composite structure [84–86]. The band at 867 cm^{-1} demonstrates the aromatic nature of biochar and shows vibrations of the C-H group whereas at 797 cm^{-1} shows a widening of the Ca-O bond which verifies the synthesis of BC using eggshells [87–89]. Similarly, bands appearing from 806-883 cm^{-1} in the spectra for composite samples, represent the characteristic peaks of GCN and firmly prove the carbon nitride-based structure of the composites whereby these peaks show the twisting vibrations of N-H group and intense bending vibrations of tri-s-triazine structure characteristic to GCN [90,91]. It is to be noted here that the 0.15-ABCN sample has shown two distinctive peaks which are not present in any of the other samples. These peaks appear at 972 cm^{-1} and 1823 cm^{-1} representing vibrations of the Ag-N group and also representing Ag-Ag bonding due to increased concentration of Ag dopant which may have negative effects on photocatalytic activity of the composite [92,93].

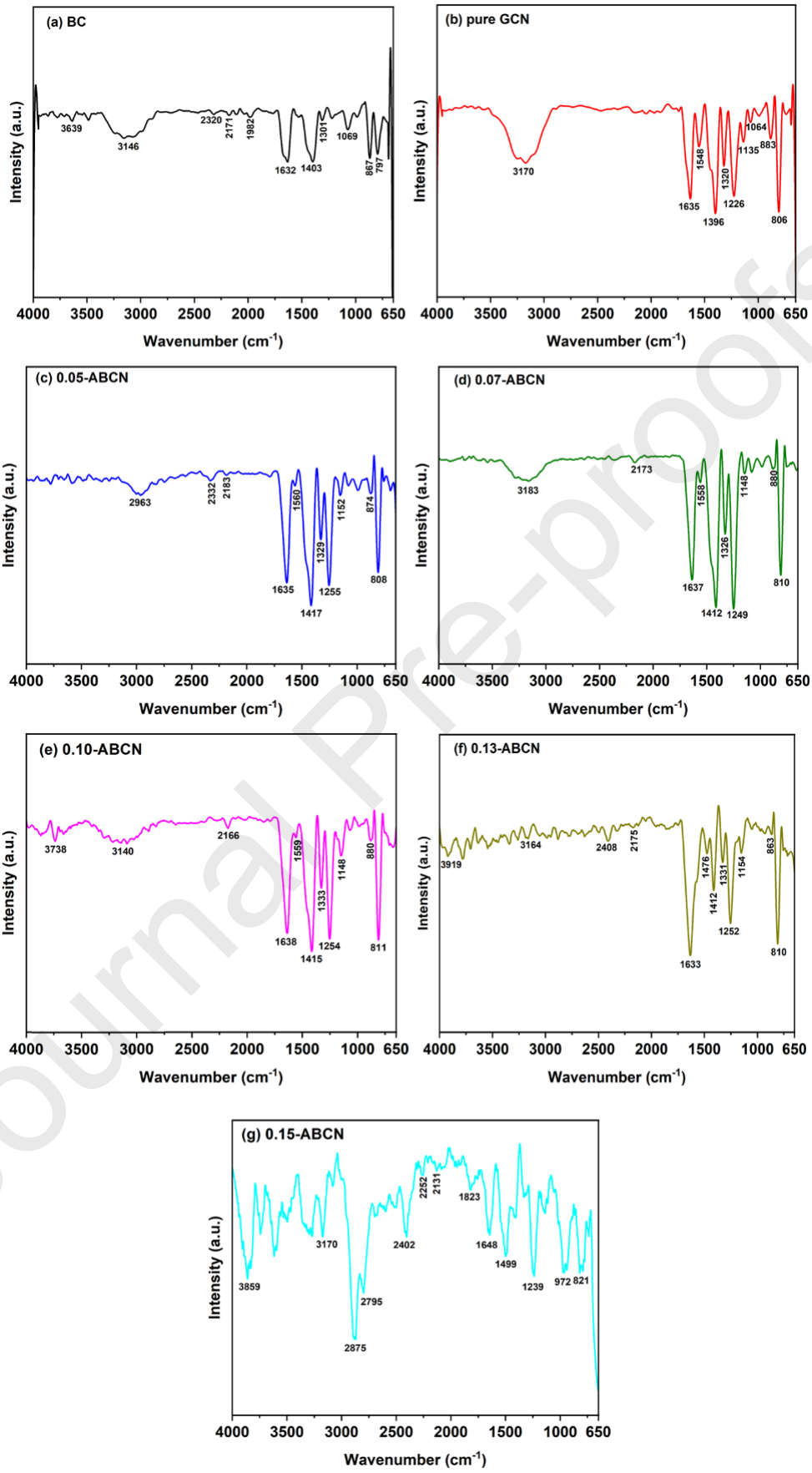

Figure 2. FTIR spectra for (a) BC, (b) pure GCN, and (c-g) *x*-ABCN composite photocatalyst samples (where *x* = 0.05g, 0.07g, 0.10g, 0.13g and 0.15g of $AgNO_3$).

3.3 High-resolution surface-imaging (SEM analysis)

High-resolution SEM images of the material under observation (BC, pure GCN, and *x*-ABCN samples) were obtained and analyzed as shown in Fig. 3. The surface of biochar (Fig. 3a) prepared from eggshells is uneven, flat, and irregular with few pores of different sizes. This type of morphology indicates a good surface for the adsorption of contaminants [94]. On the contrary, pure GCN (Fig. 3b) surface shows rough, stacked, clustered layers and pleats with a less porous nature thus limiting effective pollutant capturing and hence requiring structural modification [95]. SEM images of *x*-ABCN composite photocatalyst samples (Fig. 3c-g) reveal that all samples show porous, clustered, rough, and pleat-like morphology with the presence of BC particles well sandwiched between the layered structure of GCN [96,97]. The image contrast of composite samples is observed to increase with the increase in Ag concentration, and the most heavily contrast image is of the 0.15-ABCN sample. This increase in contrast and bright spots represents the presence and increase of Ag particles in the composite photocatalyst samples [98,99]. It is also noted that as the concentration of Ag is increased, the smooth, ordered, and bedded layer morphology of the composite samples increases which can be attributed to the delamination effect limiting the formation of bulky surfaces through modification in urea structure during thermal polycondensation process [100,101].

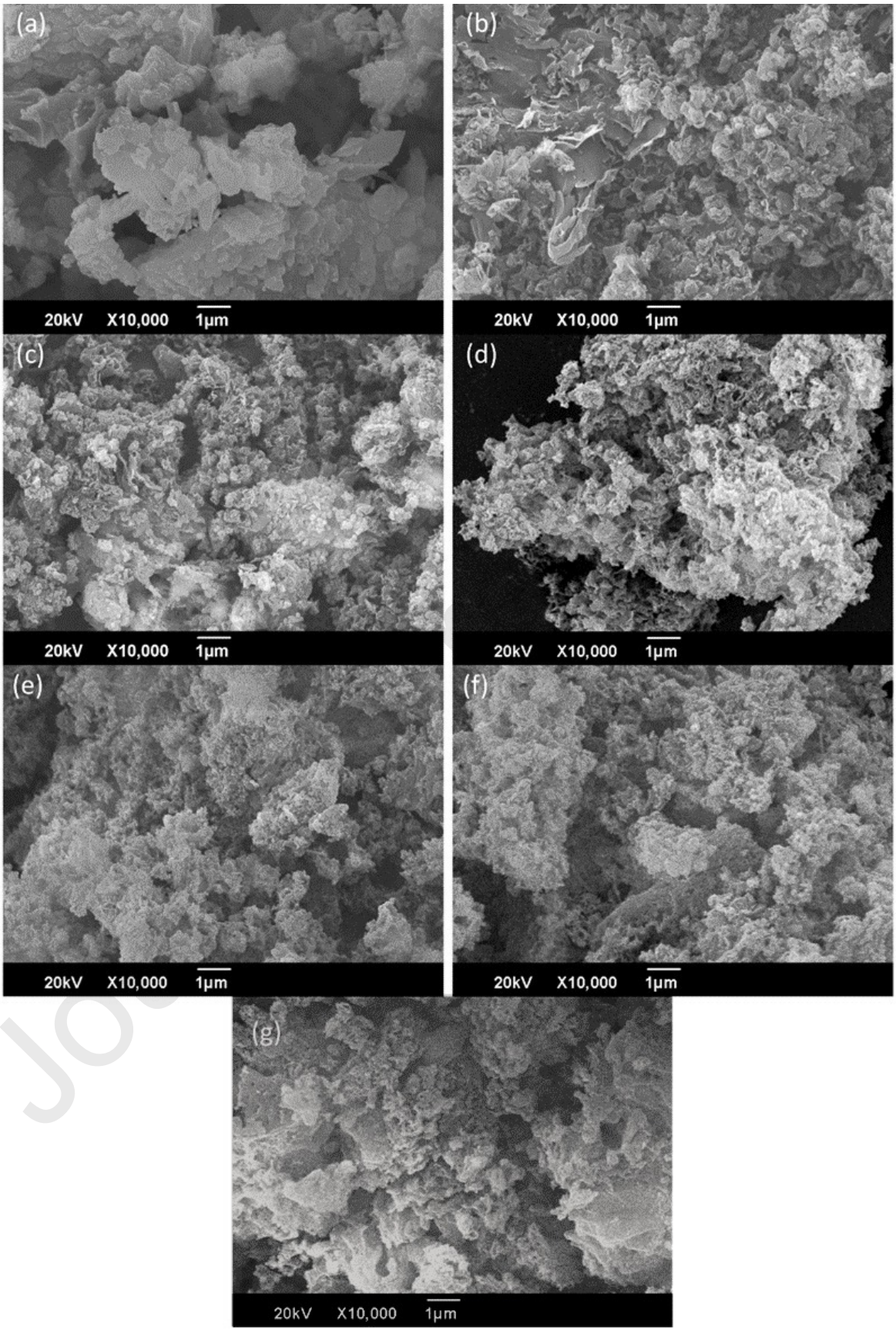
(a)
20kV X10,000 1μm
(b)
20kV X10,000 1μm
(c)
20kV X10,000 1μm
(d)
20kV X10,000 1μm
(e)
20kV X10,000 1μm
(f)
20kV X10,000 1μm
(g)
20kV X10,000 1μm

Figure 3. High-resolution SEM images of (a) BC, (b) pure GCN (c) 0.05-ABCN, (d) 0.07-ABCN, (e) 0.10-ABCN, (f) 0.13-ABCN and (g) 0.15-ABCN.

3.4 Optical absorption and band gap calculation

The optical absorption of the prepared samples was obtained using -VIS DRS spectra of powdered BC, pure GCN, and *x*-ABCN samples, and is shown in Fig 4. It is observed that the BC sample exhibits a significant absorption in the visible range (400-700 nm), with an absorption band within 300-370 nm due to the carboxyl groups presence. The pure GCN exhibits an absorption edge around 460 nm, whereas in *x*-ABCN composite photocatalyst samples, the absorption edge shifts towards the red region (visible region) with the addition of BC and Ag dopant. The well-established phenomenon that metal nanoparticles readily absorb light and result in an extension of absorption in visible region ascribed to surface plasmonic resonance (SPR) [102]. However, in the present work, such a characteristic peak of SPR is not found in any composite photocatalyst samples, the possible reason might be small Ag particles and their homogeneous distribution across the photocatalyst. Due to this, the SPR peak is buried under the strong absorption peak of GCN and BC which increases light harvesting of Ag particles consequently improving photocatalytic efficiency [103]. Despite all circumstances, the movement of the peak edge towards the red region or visible region (λ = 380-700 nm) represents the successful loading of Ag particles for *x*-ABCN samples [104,105].

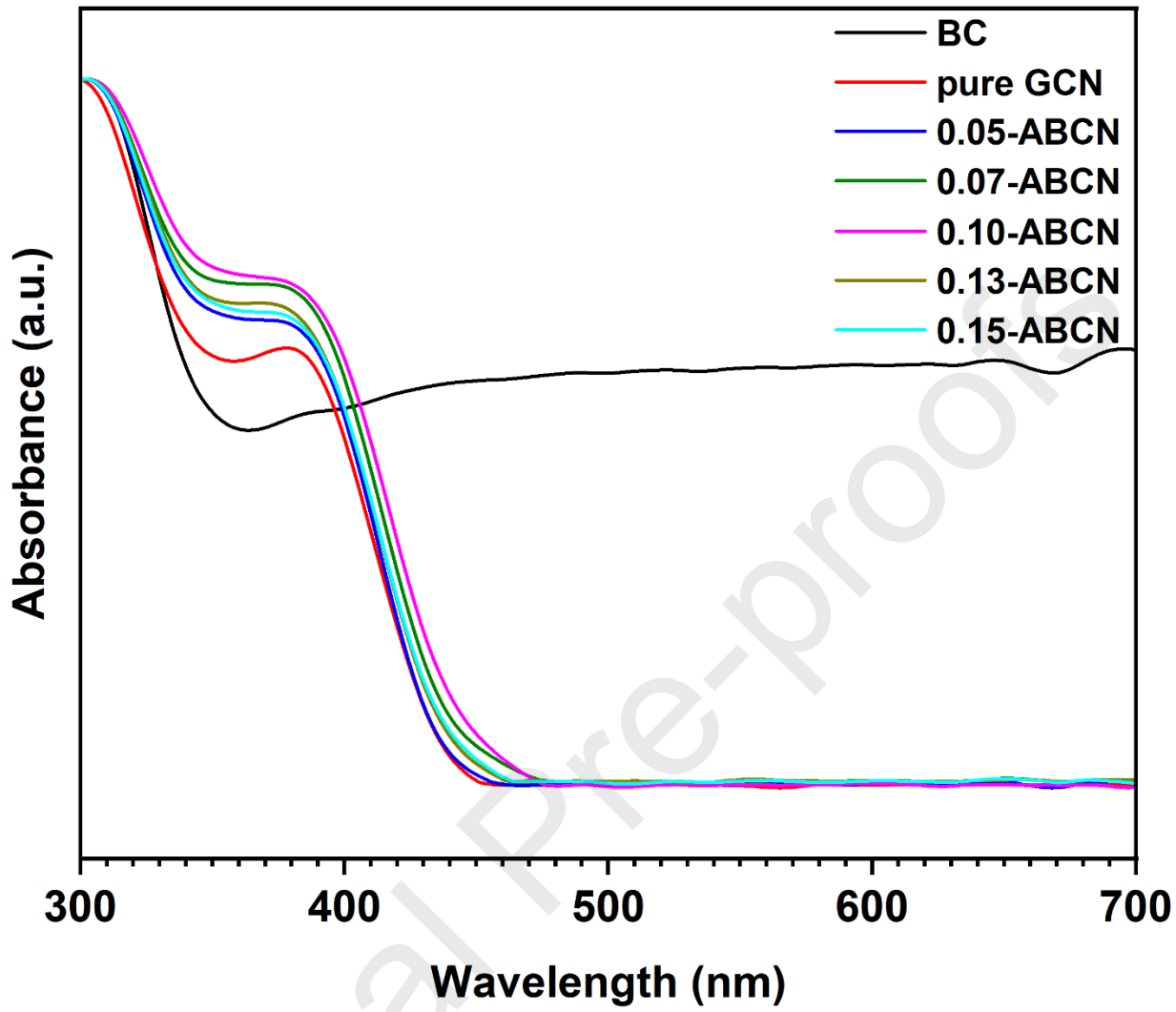

Figure 4. UV Vis DRS spectra of BC, pure GCN, and *x*-ABCN (where *x* = 0.05g, 0.07g, 0.10 g, 0.13g, and 0.15g of $AgNO_3$) composite photocatalyst samples.

The indirect band gaps of all the samples were calculated using Tauc's relation (Equation 1) and are shown in Fig. 5. After the addition of BC and Ag in the structure of pure GCN, the band gap value decreased from 2.72 eV of pure GCN to 2.66 eV, 2.58 eV, 2.53 eV, 2.61 eV, and 2.62 eV of composite samples [106,107]. Moreover, the band gap energy is abridged when Ag slowly substitutes the nitrogen in the triazine ring of GCN to create composites and increases due to the increase in Ag concentration affecting the photocatalytic activity [108,109]. The enhancement in the band gap is because of two reasons. Primarily, because of the heavy doping of the photocatalyst, additional energy states are created within the band gap which requires electron to occupy a vacant level in the conduction band. This kind of unique electronic behavior is called the Burnstein-Moss (BM) effect and is typically used to elucidate the changes in band gap as a function of dopant concentration. Furthermore, Ag induces metallic crystallization phenomenon

which increases the crystallinity in the photocatalyst, modifies the band gap, and resultantly enhances overall photocatalytic performance [110,111].

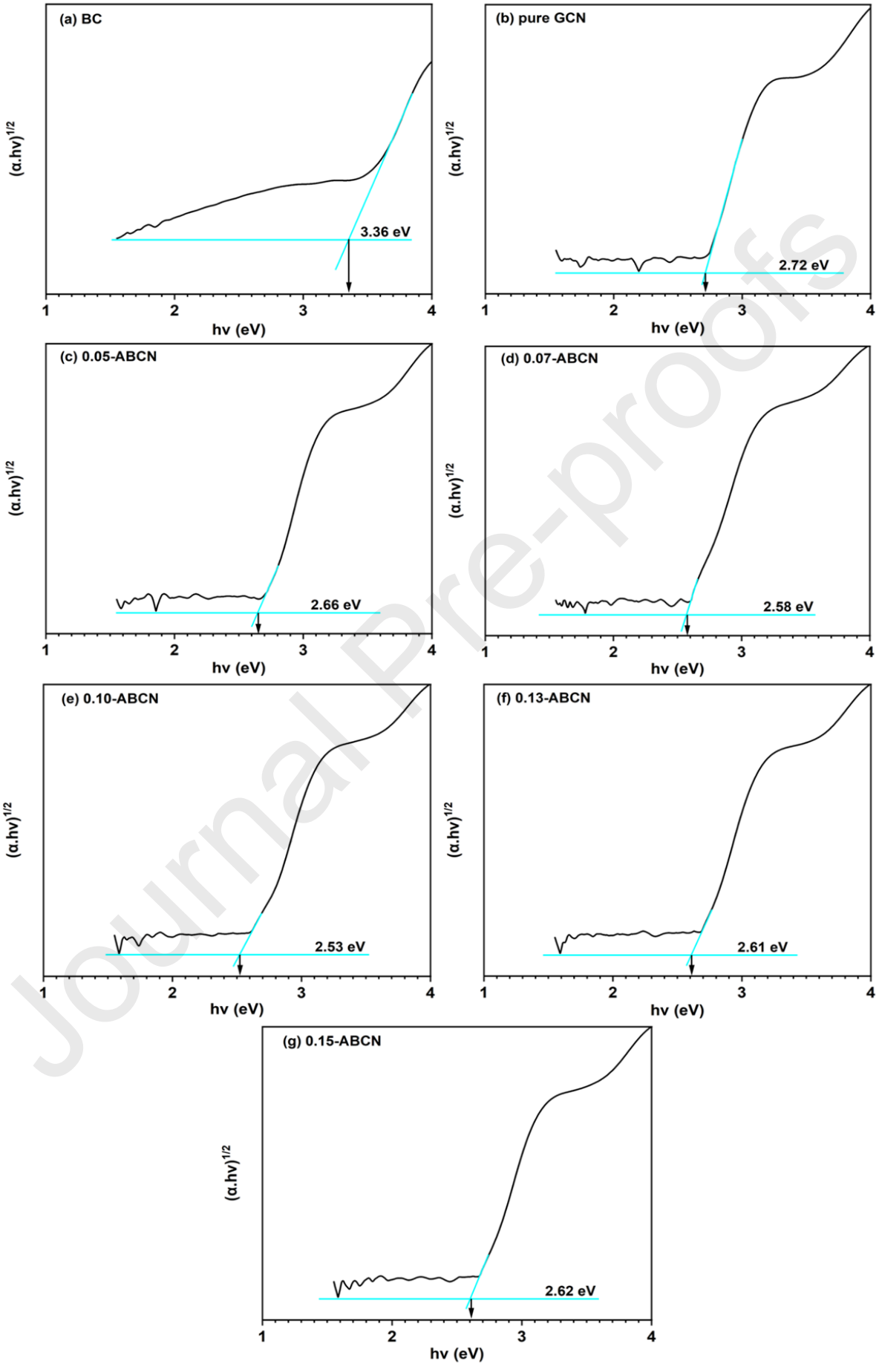

Figure 5. Estimated band gaps using Tauc's equation for (a) BC, (b) pure GCN, (c) 0.05-ABCN, (d) 0.07-ABCN, (e) 0.10 ABCN, (f) 0.13-ABCN and (g) 0.15-ABCN samples.

3.5 Photoluminescence (PL) spectroscopy analysis

The rate of electron-hole recombination is assessed with the help of Photoluminescence (PL) spectroscopy [112]. Fig. 6 shows the PL emission spectra of pure GCN and *x*-ABCN composite photocatalyst samples. It is evident, that pure GCN shows solitary emission spectra at 620 nm, while composite samples display two peaks, main peak appearing at 588 nm with an adjacent shoulder peak at 637 nm, respectively [113]. The first peak can be associated with the band-to-band recombination of photogenerated charges, second peak is attributed to the recombination of charges trapped at defect energy levels within the band gap induced by dopant in the GCN structure [107,112]. It can be observed that with increase of Ag concentration from 0.05-ABCN to 0.10-ABCN shows quenching of both emission peaks indicating the enhanced photogenerated charge extraction within these samples. Such decrease in PL intensity can be ascribed to the BC network because of the creation of Ag-doped GCN/biochar heterojunction, photogenerated charge carriers could be effectively moved from GCN or Ag-GCN to biochar, improving photoexcited charges separation. On the contrary, when Ag concentration is further increased i.e. in 0.13-ABCN and 0.15-ABCN samples, the PL emission peaks are increased instead of decreasing. Such an increase in peak strength can be referred to as excessive/unnecessary doping of Ag which increased the amount of energy levels to such an extent that they started acting as only trapping centers. Such excessive doping might also result in declined photocatalytic performance [114]. Hence, PL spectra also provide clues for Ag dopant optimization in the composite photocatalyst sample expressing a certain cut-off Ag amount where the photocatalytic performance will lead to best and then decline by restricting factors. Thus increase in peak strength of PL spectra for 0.13-ABCN and 0.15-ABCN samples can also be due to the surface poisoning of composites (0.13-ABCN and 0.15-ABCN) through increased Ag concentration which resulted in energy levels only behaving as electron trapping centers [115,116].

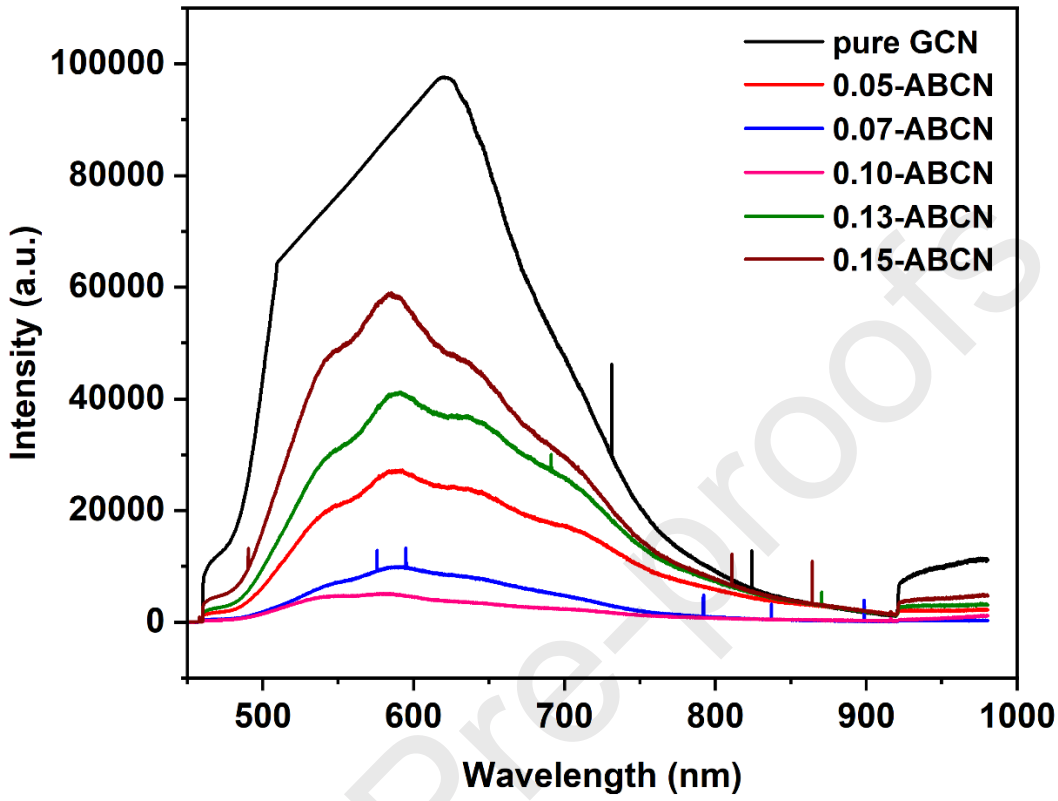

Figure 6. Photoluminescence (PL) spectra for pure GCN and *x*-ABCN (where *x* = 0.05g, 0.07g, 0.10 g, 0.13g, and 0.15g of $AgNO_3$) composite photocatalyst samples.

3.6 Evaluation of the photocatalytic activity of the prepared samples

The photocatalytic performance of the prepared samples is evaluated against the degradation of CIP-contaminated wastewater under visible light irradiation. The degradation curves, for percentage degradation and change in concentration of CIP *vs.* irradiation time, are obtained experimentally and shown in Fig. 7. A decline in the CIP concentration under dark (initial 60 minutes) can be because of simple adsorption and is deliberately proceeded to achieve an adsorption-desorption equilibrium. Upon light irradiation, a significant decline in CIP concentration is observed because of photocatalytic reactions occurring on the surface of the composite photocatalysts. The degradation curves (Fig. 7a & b) show maximum degradation efficiency for sample 0.10-ABCN after 4 h of light irradiation. The graphs showed a 70 % degradation of CIP in the case of 0.10-ABCN which is approximately 3 times as pure GCN. The arrangement of photocatalytic degradation of CIP by pure GCN and *x*-ABCN composite photocatalyst samples follows sequence 0.1-ABCN > 0.07-ABCN > 0.05-ABCN > 0.13-ABCN > 0.15-ABCN > pure GCN. It is also observed that the increase of Ag content after a certain amount, i.e. in composite samples like 0.13-ABCN and 0.15-ABCN decreases the photocatalytic performance as evidenced by the CIP degradation. This decrease in photocatalytic efficiency can be attributed to the trapping of photogenerated charges by recombination centers created which are excessively generated due to increased doping of Ag [115]. Another reason for reduced photocatalytic activity can be the surplus Ag content increasing the light opacity and making it difficult for GCN structure to absorb light thus reducing photocatalytic efficiency [117]. To further analyze the photocatalytic activity of the prepared samples, a better understanding of the process is achieved by the calculation of rate constant (k) using equation 3. Pseudo-first order kinetics is considered for the calculation of the rate constant and is listed in Table 2. The calculated rate-constants (k) show superlative photodegradation performance for 0.1-ABCN as it showed a rate constant value of 0.00334 min^{-1} which is the highest among all samples.

The improved photocatalytic performance of the *x*-ABCN composite photocatalyst samples can be attributed to enhanced light absorbance and effective photogenerated charge separation on behalf of increased Ag concentration in the composite samples to a certain extent [105]. The shifting of light absorption edge towards the red region is referred to as Ag content in the composite that has not only enhanced the visible light absorbance but also created energy levels that are effectively trapping electrons and reducing charges recombination [118]. A large amount of photogenerated charges are produced due to the narrowing of the band gap ensuring improvement in overall light absorbance of the composites [119]. Another important reason for the effective degradation of CIP is the presence of BC in the structure of GCN [120]. As depicted by PL spectra, BC networks in the composite photocatalysts may provide an efficient conductive pathway to extract the photogenerated charges leading to improved reactivity with adsorbed CIP and intermediate species. However, there is an optimum value of Ag and BC that strongly harmonizes with the improved charge separation with enhanced visible light absorbance in the case of 0.10-ABCN.

As reported, CIP during degradation is transformed into many transitional species before the final mineralization into water and carbon dioxide[121]. Such transitional species were identified with the help of LC-MS suggesting certain degradation pathways [121]. According to the relevant study, two reactive oxygen species $O_2^{\bullet -}$ and $OH^{\bullet}$ are considered key species for the CIP transformation and complete mineralization of CIP. Hence, based on the reported literature,

possible mechanism for CIP degradation is depicted in Fig. 8. In general, the photocatalytic degradation of pollutants at the photocatalyst surface mainly comprises of the absorption of light by photocatalyst, photogeneration of charge carriers, conveyance of photogenerated charges (electron-hole pairs) to the surface, followed by surface oxidation-reduction reactions with pollutants adsorbed [122]. CIP photocatalytic degradation can be interpreted in a similar manner, when the light irradiates the photocatalyst (which is well suspended in CIP contaminated water), photoexcited electron-hole pairs are generated. The photogenerated electrons move to the conduction band whereas the holes to the valence band. The photogenerated electrons can move to photocatalyst's surface as well as extracted by BC and Ag contents, and reduce the adsorbed O_2 to $O_2^{\bullet-}$, whereas the photogenerated holes reacts with adsorbed H_2O molecules to generate OH•. Such radicals and generated species react with the CIP molecules present in the solution and/or adsorbed CIP on photocatalyst surface to transform into various transitional species, ultimately leading to partial or complete mineralization of CIP into water and carbon dioxide. Furthermore, the photogenerated charges can also directly oxidize the CIP to degradation products, either in solution or adsorbed on photocatalyst surface. As observed, the presence of BC and Ag in the photocatalysts enhances the photocatalytic performance which can be mainly ascribed to the improved optical absorption and photogenerated charges separation. The Ag content mainly contributed to enhanced visible light absorption, which lead to enhanced photogenerated charges. Whereas BC role can be mainly attributed to providing a conductive pathway for photogenerated charges leading to improved charges separation and faster reaction with CIP. Hence, both Ag and BC contributed significantly to photocatalytic performance of the prepared composite photocatalysts in the present work. Different reactions engaged in the degradation of CIP are presented in equation 4-10 [28,123,124].

$$ABCN \xrightarrow{hv} ABCN\left(e_{CB}^{-}\right) + ABCN\left(h_{VB}^{+}\right) \quad (4)$$

$$ABCN(e_{CB}^{-}) + O_2 \rightarrow O_2^{\bullet-} \quad (5)$$

$$2O_2^{\bullet-} + 2H^{+} \rightarrow H_2O_2 \quad (6)$$

$$ABCN(e_{CB}^{-}) + H_2O_2 \rightarrow OH^{\bullet} + OH^{-} \quad (7)$$

$$ABCN\left(h_{VB}^{+}\right) + OH^{-} \rightarrow OH^{\bullet} + ABCN \quad (8)$$

$$CIP + OH^{\bullet} \rightarrow Degradation\ products \quad (9)$$

$$CIP + O_2^{\bullet-} \rightarrow Degradation\ products \quad (10)$$

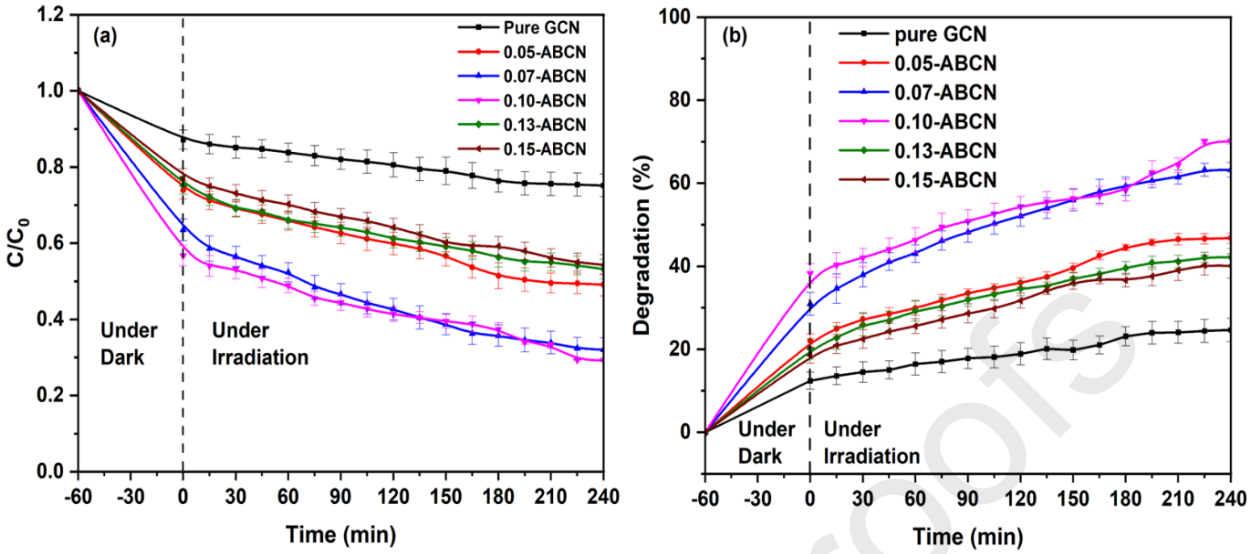

Figure 7. Photocatalytic performance evaluation via., (a) Change in CIP concentration *vs.* time, and (b) CIP degradation efficiency *vs.* time, exhibited by pure GCN and *x*-ABCN samples.

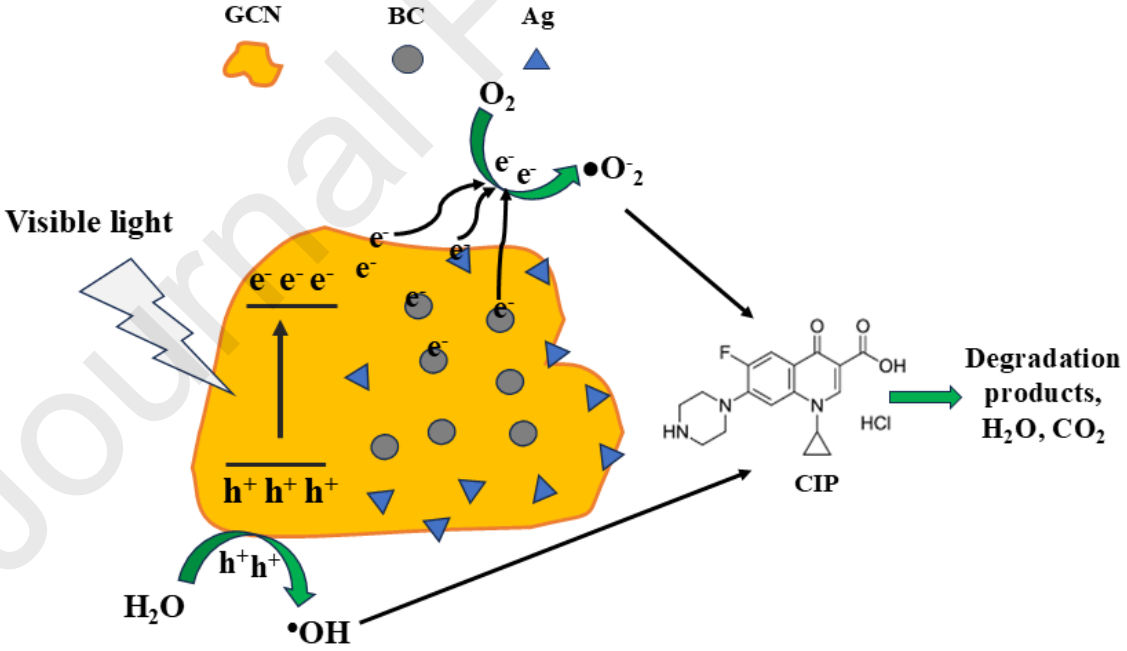

Figure 8. Proposed mechanism of CIP photodegradation at the surface of *x*-ABCN photocatalyst sample.

Table 2. Rate constants (*k*) for CIP degradation employing pure GCN and *x*-ABCN composite photocatalyst samples.

Photocatalyst	Rate constant *k* (min^{-1})
Pure GCN	0.000800724
0.05-ABCN	0.002086052
0.07-ABCN	0.003213452
0.10-ABCN	0.003348159
0.13-ABCN	0.001717967
0.15-ABCN	0.001699311

To investigate the changes for the spent pattern for the optimal (showing best after 3 cycles of CIP in Fig. 9. It can be pattern of the spent 0.10- compared to XRD of doesn't exhibit any peaks and/or appearance XRD results clearly samples show no major after 3 experimental stability of the crystalline structure photocatalyst, XRD sample i.e. 0.10-ABCN performance) is obtained degradation and shown observed that the XRD ABCN sample as fresh 0.10 ABCN, significant changes in of new peaks. Thus, the show that 0.10-ABCN change and are stable cycles confirming the photocatalyst.

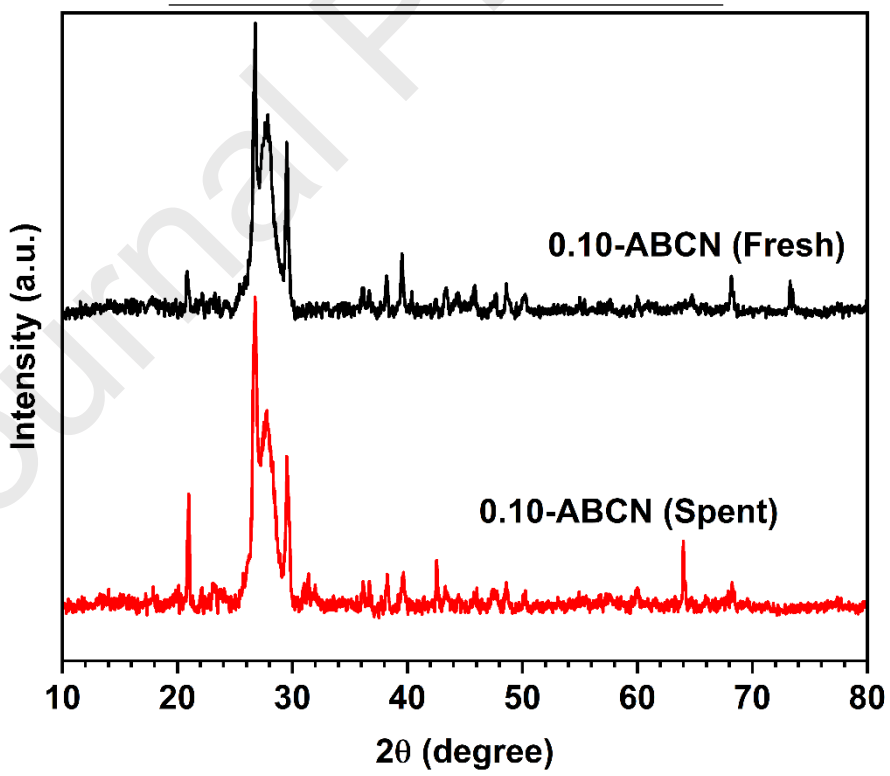

Figure 9. XRD patterns of fresh 0.10-ABCN and spent 0.10-ABCN (used for 3 cycles of CIP degradation) samples.

4.0 Conclusions

The composite photocatalysts composed of Ag-doped GCN coupled with biochar (BC) were successfully synthesized by adopting a facile synthesis strategy. The composite photocatalysts synthesis was based on approaches of doping strategy for extension and enhancement of optical absorbance and coupling with carbonaceous material i.e. biochar for efficient separation of photogenerated charges. Different composite photocatalysts were synthesized with varied content of Ag dopant in GCN but with fixed amount of BC (termed as *x*-ABCN). The photocatalytic performance of the prepared composite photocatalysts was evaluated against the degradation of CIP antibiotic-contaminated wastewater under a 5W white LED light irradiation. Results showed the best photocatalytic degradation activity of CIP for the 0.1-ABCN sample (sample with 10 wt.% Ag content). The enhanced photocatalytic activity is mainly because of the optimum loading of Ag and BC in the framework of GCN, where Ag improved the optical absorbance of GCN, and BC improved the charge separation and transferring capability to the surface for reaction with CIP adsorbed at the surface pores of the photocatalyst and/or in the solution. The improvement in optical absorption of GCN is mainly ascribed to the narrowing down of bandgap due to Ag doping till the optimum level i.e. for 0.1 ABCN sample. Beyond 0.1-ABCN, the photocatalytic activity is reduced which is due to the reason of excessive loading of Ag generating a lot of energy levels in the band gap, merely acting as electron trapping centers. Further, the coupling of biochar with the Ag-doped GCN enhances the photogenerated charge separation as exhibited by PL spectra thus contributing to the overall improvement in photocatalytic performance. The present work suggests the formation of composite photocatalysts based on ternary components and/or merging of various synthesis approaches provides a facile and cost-effective approach in achieving a visible light active and efficient photogenerated charges separation. It is believed the present study is a fruitful endeavor in the field of AOPs for wastewater treatment by the development of visible light active composite photocatalyst based on ternary components i.e. Ag, GCN, and BC for effective and economical removal of pharmaceutical micropollutants.

Acknowledgement : This research was supported by Higher Education Commission of Pakistan(HEC) through project HEC-NRPU (2017)-7924, and "Regional Innovation Strategy (RIS)" through the National Research Foundation of Korea(NRF) funded by the Ministry of Education(MOE)(2023-RIS009).

5.0 References

1 B. Sarker, K. N. Keya, F. I. Mahir, K. M. Nahiun, S. Shahida and R. A. Khan, *Guigoz. Sci. Rev.*, 2021, 32–41.

2 C. Gadipelly, A. Pérez-González, G. D. Yadav, I. Ortiz, R. Ibáñez, V. K. Rathod and K. V. Marathe, *Ind. Eng. Chem. Res.*, 2014, **53**, 11571–11592.

3 K. Elsaid, V. Olabi, E. T. Sayed, T. Wilberforce and M. A. Abdelkareem, *J. Environ. Manage.*, 2021, **292**, 112694.

4 L. K. Abia Akebe, T. Sibanda, R. Selvarajan, M. A. El-Liethy and I. Kamika, *Front. Environ. Sci.*, 2022, **10**, 1–2.

5 Z. Wang, Y. Muhammad, R. Tang, C. Lu, S. Yu, R. Song, Z. Tong, B. Han and H. Zhang, *Sep. Purif. Technol.*, 2021, **274**, 119059.

6 A. Sonune and R. Ghate, *Desalination*, 2004, **167**, 55–63.

7 Z. hua Liu, Y. Kanjo and S. Mizutani, *Sci. Total Environ.*, 2009, **407**, 731–748.

8 B. Swanckaert, J. Geltmeyer, K. Rabaey, K. De Buysser, L. Bonin and K. De Clerck, *Sep. Purif. Technol.*, 2022, **287**, 120529.

9 H. Honda, H. Takamatsu and J. J. Wei, *Nihon Kikai Gakkai Ronbunshu, B Hen/Transactions Japan Soc. Mech. Eng. Part B*, 1972, **68**, 2327–2332.

10 D. Zhou, D. Li and Z. Chen, *Front. Chem.*, 2024, **12**, 1–18.

11 K. Qi, S. Y. Liu and M. Qiu, *Cuihua Xuebao/Chinese J. Catal.*, 2018, **39**, 867–875.

12 M. Sivachidambaram, J. J. Vijaya, K. Kaviyarasu, L. J. Kennedy, H. A. Al-Lohedan and R. Jothi Ramalingam, *RSC Adv.*, 2017, **7**, 38861–38870.

13 C. Maria Magdalane, K. Kaviyarasu, N. Matinise, N. Mayedwa, N. Mongwaketsi, D. Letsholathebe, G. T. Mola, N. AbdullahAl-Dhabi, M. V. Arasu, M. Henini, J. Kennedy, M. Maaza and B. Jeyaraj, *South African J. Chem. Eng.*, 2018, **26**, 49–60.

14 K. Qi, B. Cheng, J. Yu and W. Ho, *J. Alloys Compd.*, 2017, **727**, 792–820.

15 S. K. Jesudoss, J. Judith Vijaya, P. Iyyappa Rajan, K. Kaviyarasu, M. Sivachidambaram, L. John Kennedy, H. A. Al-Lohedan, R. Jothiramalingam and M. A. Munusamy, *Photochem. Photobiol. Sci.*, 2017, **16**, 766–778.

16 P. Gholami, A. Khataee, R. D. C. Soltani and A. Bhatnagar, *Ultrason. Sonochem.*, 2019, **58**, 104681.

17 M. Qiu, R. Wang and X. Qi, *J. Taiwan Inst. Chem. Eng.*, 2019, **102**, 394–402.

18 K. Qi, Y. Xie, R. Wang, S. yuan Liu and Z. Zhao, *Appl. Surf. Sci.*, 2019, **466**, 847–853.

19 A. Verma, G. Sharma, T. Wang, A. Kumar, P. Dhiman and A. García-Peñas, *Carbon Lett.*, , DOI:10.1007/s42823-024-00811-4.

20 K. Qi, S. yuan Liu and A. Zada, *J. Taiwan Inst. Chem. Eng.*, 2020, **109**, 111–123.

21 C. Xue, P. Wang, H. Che, W. Liu, B. Liu and Y. Ao, *Appl. Catal. B Environ.*, 2024, **340**, 123259.

22 C. Naga Lakshmi, M. Irfan, R. Sinha and N. Singh, *Environ. Res.*, 2024, **242**, 117812.

23 S. Ganesan, T. Kokulnathan, S. Sumathi and A. Palaniappan, *Sci. Rep.*, 2024, **14**, 1–13.

24 X. Gao, Q. Li, Y. Wang, Q. Wei, S. Cui and Z. Nie, *Appl. Surf. Sci.*, 2024, 159574.

25 O. Oluseun Akintunde, J. Hu, M. Golam Kibria, S. Pogosian and G. Achari, *Chemosphere*, 2023, **344**, 140287.

26 N. Zhang, L. Wen, J. Yan and Y. Liu, *Chem. Pap.*, 2020, **74**, 389–406.

27 L. Jiang, X. Yuan, Y. Pan, J. Liang, G. Zeng, Z. Wu and H. Wang, *Appl. Catal. B Environ.*, 2017, **217**, 388–406.

28 I. Idrees, A. Razzaq, M. Zafar, A. Umer, F. Mustafa, F. Rehman and W. Young, *Arab. J. Chem.*, 2024, **17**, 105615.

29 Y. Yuan, W. L. Wang, Z. W. Wang, J. Wang and Q. Y. Wu, *J. Environ. Sci. (China)*, 2024, **139**, 12–22.

30 D. Dey, T. Shafi, S. Chowdhury, B. K. Dubey and R. Sen, *Chemosphere*, 2024, **351**, 141164.

31 J. Sun, B. Zhang, W. Chen, Z. Tao, J. Liu and L. Wang, *Carbon N. Y.*, 2023, **209**, 117988.

32 Y. Zhou, S. Y. Leong and Q. Li, *J. Water Process Eng.*, 2023, **55**, 104222.

33 F. Xu, N. An, C. Lai, M. Zhang, B. Li, S. Liu, L. Li, L. Qin, Y. Fu, H. Yi and H. Yan, *Chemosphere*, 2022, **293**, 133648.

34 D. R. Rout, S. Chaurasia and H. M. Jena, *J. Environ. Manage.*, 2022, **318**, 115449.

35 K. Pandi, M. Preeyanghaa, V. Vinesh, J. Madhavan and B. Neppolian, *Environ. Res.*, 2022, **207**, 112188.

36 F. Du, Z. Lai, H. Tang, H. Wang and C. Zhao, *Chemosphere*, 2022, **287**, 132391.

37 T. Zhou, G. Dong, J. Geng, K. Han and C. Xiao, *Appl. Surf. Sci.*, 2024, **655**, 159592.

38 X. Liu, Z. Cheng, L. Lin, W. Xu, S. Chen and H. Zhuang, *Diam. Relat. Mater.*, 2024, **148**, 111376.

39 X. Sun, Z. Zheng, J. Ma, T. Xian, G. Liu and H. Yang, *Appl. Surf. Sci.*, 2024, **653**, 159421.

40 L. Shi, L. Liang, F. Wang, M. Liu, K. Chen, K. Sun, N. Zhang and J. Sun, *ACS Sustain. Chem. Eng.*, 2015, **3**, 3412–3419.

41 Z. Zhao, Y. Ma, J. Fan, Y. Xue, H. Chang, Y. Masubuchi and S. Yin, *J. Alloys Compd.*, 2018, **735**, 1297–1305.

42 T. K. Mukhopadhyay, L. Leherte and A. Datta, *J. Phys. Chem. Lett.*, 2021, **12**, 1396–1406.

43 X. Li, J. Zhang, L. Shen, Y. Ma, W. Lei, Q. Cui and G. Zou, *Appl. Phys. A Mater. Sci. Process.*, 2009, **94**, 387–392.

44 S. Shailendrakumar, R. Chava, S. Appari, A. Bahurudeen, B. Vardhan and R. Kuncharam, *J. Environ. Chem. Eng.*, 2022, **10**, 106899.

45 A. Sarwar, A. Razzaq, M. Zafar, I. Idrees, F. Rehman and W. Y. Kim, *Results Phys.*, 2023, **45**, 106253.

46 J. Krýsa, K. Bouzek and C. Stollberg, *J. Appl. Electrochem.*, 2000, **30**, 1033–1041.

47 S. Chakrabarti and B. K. Dutta, *J. Hazard. Mater.*, 2004, **112**, 269–278.

48 H. D. E. Cálcio, E. Baseado and E. M. Evidências, 2003, **11**, 269–282.

49 J. F. T. Pierson and C. Rousselot, 2005, **200**, 276–279.

50 C. A. Osagiede and F. A. Aisien, *Fuel*, 2024, **358**, 130076.

51 M. H. Derkani, A. J. Fletcher, M. Fedorov, W. Abdallah, B. Sauerer, J. Anderson and Z. J. Zhang, *Colloids and Interfaces*, , DOI:10.3390/colloids3040062.

52 T. Fazal, A. Razzaq, F. Javed, A. Hafeez, N. Rashid, U. S. Amjad, M. S. Ur Rehman, A. Faisal and F. Rehman, *J. Hazard. Mater.*, 2020, **390**, 121623.

53 L. Luo, A. Zhang, M. J. Janik, K. Li, C. Song and X. Guo, *Appl. Surf. Sci.*, 2017, **396**, 78–84.

54 T. H. Pham, Y. Myung, Q. Van Le and T. Y. Kim, *Chemosphere*, 2022, **301**, 134626.

55 T. H. Pham, S. H. Jung and T. Y. Kim, *Sol. Energy*, 2021, **224**, 18–26.

56 M. Zhang, J. Xu, R. Zong and Y. Zhu, *"Applied Catal. B, Environ.*, 2014, **147**, 229–235.

57 H. Xu, C. Wang, Y. Song, J. Zhu, Y. Xu, J. Yan, Y. Song and H. Li, *Chem. Eng. J.*, 2014, **241**, 35–42.

58 J. Zhao, Z. Yang, C. Yu, J. Qiu and Z. Song, *Chem. Eng. J.*, 2018, **341**, 175–186.

59 Y. Bu, Z. Chen and W. Li, *Appl. Catal. B Environ.*, 2014, **144**, 622–630.

60 L. Ge, C. Han and J. Liu, *Appl. Catal. B Environ.*, 2011, **108**–**109**, 100–107.

61 C. Han, L. Ge, C. Chen, Y. Li, Z. Zhao, X. Xiao, Z. Li and J. Zhang, *J. Mater. Chem. A*, 2014, **2**, 12594–12600.

62 W. Liu, M. Wang, C. Xu and S. Chen, *Chem. Eng. J.*, 2012, **209**, 386–393.

63 K. Sridharan, E. Jang and T. J. Park, *Appl. Catal. B Environ.*, 2013, **142**–**143**, 718–728.

64 Y. Tian, B. Chang, J. Fu, B. Zhou, J. Liu, F. Xi and X. Dong, *J. Solid State Chem.*, 2014, **212**, 1–6.

65 M. R. Miroliaei, A. Dadfarma, M. Shahabi-Nejad, E. Jalali and H. Sheibani, *Brazilian J. Chem. Eng.*, , DOI:10.1007/s43153-023-00374-3.

66 R. Wang, X. Lan, T. Zhou, X. Qian, B. Qu, P. Lv and Y. Wang, *J. Food Compos. Anal.*, 2024, **125**, 105824.

67 C. Xu, R. Liu, L. Chen and Q. Wang, *Materials (Basel).*, , DOI:10.3390/ma16175873.

68 L. Pi, R. Jiang, W. Zhou, H. Zhu, W. Xiao, D. Wang and X. Mao, *Appl. Surf. Sci.*, 2015, **358**, 231–239.

69 A. Subashini, P. Varun Prasath, S. Sagadevan, J. Anita Lett, I. Fatimah, F. Mohammad, H. A. Al-Lohedan, S. F. Alshahateet and W. Chun Oh, *Chem. Phys. Lett.*, 2021, **769**, 138441.

70 A. Kharlamov, M. Bondarenko and G. Kharlamova, *Diam. Relat. Mater.*, 2016, **61**, 46–55.

71 Y. Duan, L. Deng, Z. Shi, X. Liu, H. Zeng, H. Zhang and J. Crittenden, *J. Colloid Interface Sci.*, 2020, **561**, 696–707.

72 R. Zhang, X. Zhang, S. Liu, J. Tong, F. Kong, N. Sun, X. Han and Y. Zhang, *Mater. Res. Bull.*, 2021, **140**, 111263.

73 H. Sereshti, E. Beyrak-Abadi, M. Esmaeili Bidhendi, I. Ahmad, S. Shahabuddin, H. Rashidi Nodeh, N. Sridewi and W. N. Wan Ibrahim, *Nanomaterials*, , DOI:10.3390/nano12203576.

74 L. Zhang, Z. Jin, S. Huang, X. Huang, B. Xu, L. Hu, H. Cui, S. Ruan and Y. J. Zeng, *Appl. Catal. B Environ.*, 2019, **246**, 61–71.

75 M. Tripathy, S. Padhiari, S. Kar, G. Hota and A. K. Ghosh, *Appl. Surf. Sci.*, 2022, **583**, 152443.

76 C. H. Chia, B. Gong, S. D. Joseph, C. E. Marjo, P. Munroe and A. M. Rich, *Vib. Spectrosc.*, 2012, **62**, 248–257.

77 Z. Xiong, Z. Shihong, Y. Haiping, S. Tao, C. Yingquan and C. Hanping, *Bioenergy Res.*, 2013, **6**, 1147–1153.

78 F. Paquin, J. Rivnay, A. Salleo, N. Stingelin and C. Silva, *J. Mater. Chem. C*, 2015, **3**, 10715–10722.

79 J. A. Wahab, G. Xu, H. Lee, P. D. Nam, K. Wei, S. H. Kim and I. S. Kim, *Fibers Polym.*, 2016, **17**, 1776–1781.

80 K. L. Sefatlhi, V. U. Ultra and S. Majoni, *Waste and Biomass Valorization*, 2024, **15**, 283–300.

81 I. Mechnou, I. Mourtah, Y. Raji, A. Chérif, L. Lebrun and M. Hlaibi, *J. Clean. Prod.*, , DOI:10.1016/j.jclepro.2020.125649.

82 D. R. Paul, R. Sharma, P. Panchal, S. P. Nehra, A. P. Gupta and A. Sharma, *Int. J. Hydrogen Energy*, 2020, **45**, 23937–23946.

83 C. Troca-Torrado, M. Alexandre-Franco, C. Fernández-González, M. Alfaro-Domínguez and V. Gómez-Serrano, *Express Polym. Lett.*, 2022, **16**, 1280–1303.

84 S. Ma, X. Wang, S. Wang and K. Feng, *J. Soils Sediments*, 2022, **22**, 1418–1430.

85 T. Mimmo, P. Panzacchi, M. Baratieri, C. A. Davies and G. Tonon, *Biomass and Bioenergy*, 2014, **62**, 149–157.

86 Y. Zhao, D. Feng, Y. Zhang, Y. Huang and S. Sun, *Fuel Process. Technol.*, 2016, **141**, 54–60.

87 T. Bandara, J. Xu, I. D. Potter, A. Franks, J. B. A. J. Chathurika and C. Tang, *Chemosphere*, 2020, **254**, 126745.

88 M. Zhao, Y. Dai, M. Zhang, C. Feng, B. Qin, W. Zhang, N. Zhao, Y. Li, Z. Ni, Z. Xu, D. C. W. Tsang and R. Qiu, *Sci. Total Environ.*, 2020, **717**, 136894.

89 A. E. Segneanu, R. Trusca, C. Cepan, M. Mihailescu, C. Muntean, D. D. Herea, I. Grozescu and A. Salifoglou, *Nanomaterials*, , DOI:10.3390/nano13182572.

90 A. M. Bakry, W. M. Alamier, M. S. El-Shall and F. S. Awad, *J. Mater. Res. Technol.*, 2022, **20**, 1456–1469.

91 X. Long, C. Feng, S. Yang, D. Ding, J. Feng, M. Liu, Y. Chen, J. Tan, xingjie Peng, J. Shi and R. Chen, *Chem. Eng. J.*, 2022, **435**, 134835.

92 J. Kim, H. E. Kim and H. Lee, *ChemSusChem*, 2018, **11**, 104–113.

93 J. Zou, Y. Yu, K. Qiao, S. Wu, W. Yan, S. Cheng, N. Jiang and J. Wang, *J. Mater. Sci.*, 2020, **55**, 13618–13633.

94 A. Akram, S. Muzammal, M. B. Shakoor, S. R. Ahmad, A. Jilani, J. Iqbal, A. G. Al-Sehemi, A. Kalam and S. F. O. Aboushoushah, *Catalysts*, , DOI:10.3390/catal12040431.

95 T. K. A. Nguyen, T. T. Pham, H. Nguyen-Phu and E. W. Shin, *Appl. Surf. Sci.*, 2021, **537**, 148027.

96 F. Wei, J. Li, C. Dong, Y. Bi and X. Han, *Chemosphere*, 2020, **242**, 125201.

97 L. Meng, W. Yin, S. Wang, X. Wu, J. Hou, W. Yin, K. Feng, Y. S. Ok and X. Wang, *Chemosphere*, 2020, **239**, 124713.

98 D. Jembrih-Simbürger, C. Neelmeijer, O. Schalm, P. Fredrickx, M. Schreiner, K. De Vis, M. Mäder, D. Schryvers and J. Caen, *J. Anal. At. Spectrom.*, 2002, **17**, 321–328.

99 S. Agnihotri, S. Mukherji and S. Mukherji, *Nanoscale*, 2013, **5**, 7328–7340.

100 Y. Oh and M. Lee, *Appl. Surf. Sci.*, 2017, **399**, 555–564.

101 P. Navabpour, S. Ostovarpour, J. Hampshire, P. Kelly, J. Verran and K. Cooke, *Thin Solid Films*, 2014, **571**, 75–83.

102 M. Hosny, M. Fawzy and A. S. Eltaweil, *Sci. Rep.*, 2022, **12**, 1–17.

103 N. Le Minh Tri, J. Kim, B. L. Giang, T. M. Al Tahtamouni, P. T. Huong, C. Lee, N. M. Viet and D. Quang Trung, *J. Ind. Eng. Chem.*, 2019, **80**, 597–605.

104 S. Dahiya, A. Sharma and S. Chaudhary, *Environ. Sci. Pollut. Res.*, 2023, **30**, 25650–25662.

105 T. Luo, X. Hu, Z. She, J. Wei, X. Feng and F. Chang, *J. Mol. Liq.*, 2021, **324**, 114772.

106 X. S. Zhang, J. Y. Hu and H. Jiang, *Chem. Eng. J.*, 2014, **256**, 230–237.

107 S. Wen, L. Sang, G. Yang, X. He, J. Meng, D. Song and Y. Yang, *J. Alloys Compd.*, 2023, **962**, 171194.

108 N. Ahmad, A. M. Alshehri, Z. R. Khan, I. Ahmad, P. M. Z. Hasan, A. A. Melaibari and M. Shkir, *Mater. Sci. Semicond. Process.*, 2022, **137**, 106239.

109 D. Dridi, L. Bouaziz, M. Karyaoui, Y. Litaiem and R. Chtourou, *J. Mater. Sci. Mater. Electron.*, 2018, **29**, 8267–8278.

110 B. Tiss, M. Erouel, N. Bouguila, M. Kraini and K. Khirouni, *J. Alloys Compd.*, 2019, **771**, 60–66.

111 N. P. F. Gonçalves, M. A. O. Lourenço, S. R. Baleuri, S. Bianco, P. Jagdale and P. Calza, *J. Environ. Chem. Eng.*, 2022, **10**, 107256.

112 D. Das, D. Banerjee, D. Pahari, U. K. Ghorai, S. Sarkar, N. S. Das and K. K. Chattopadhyay, *J. Lumin.*, 2017, **185**, 155–165.

113 X. Wu, D. Gao, P. Wang, H. Yu and J. Yu, *Carbon N. Y.*, 2019, **153**, 757–766.

114 G. Gong, Y. Liu, B. Mao, L. Tan, Y. Yang and W. Shi, *Appl. Catal. B Environ.*, 2017, **216**, 11–19.

115 H. Zhang, J. Xu, Y. Yuan, Y. Guo, X. Tan, H. Wang, X. Hu and C. Tang, *Sep. Purif. Technol.*, , DOI:10.1016/j.seppur.2023.125520.

116 L. Lu, R. Shan, Y. Shi, S. Wang and H. Yuan, *Chemosphere*, 2019, **222**, 391–398.

117 Y. Yang, Y. Guo, F. Liu, X. Yuan, Y. Guo, S. Zhang, W. Guo and M. Huo, *Appl. Catal. B Environ.*, 2013, **142**–**143**, 828–837.

118 S. A. Ansari, M. M. Khan, M. O. Ansari and M. H. Cho, *Sol. Energy Mater. Sol. Cells*, 2015, **141**, 162–170.

119 M. Tahir, A. Sherryna, A. A. Khan, M. Madi, A. Y. Zerga and B. Tahir, *Energy & Fuels*, 2022, **36**, 8948–8977.

120 H. Sun, J. Yang, Y. Wang, Y. Liu, C. Cai and A. Davarpanah, *Coatings*, 2021, **11**, 1–23.

121 M. Chen, T. Yang, L. Zhao, X. Shi, R. Li, L. Ma, Y. Huang, Y. Wang and S. cheng Lee, *Appl. Surf. Sci.*, 2024, **645**, 158835.

122 H. Chakhtouna, A. Ouhssain, I. M. Kadmiri, H. Benzeid, N. Zari, A. el kacem Qaiss and R. Bouhfid, *J. Photochem. Photobiol. A Chem.*, , DOI:10.1016/j.jphotochem.2023.114971.

123 S. Li, T. Huang, P. Du, W. Liu and J. Hu, *Water Res.*, , DOI:10.1016/j.watres.2020.116286.

124 A. Salma, S. Thoröe-Boveleth, T. C. Schmidt and J. Tuerk, *J. Hazard. Mater.*, 2016, **313**, 49–59.

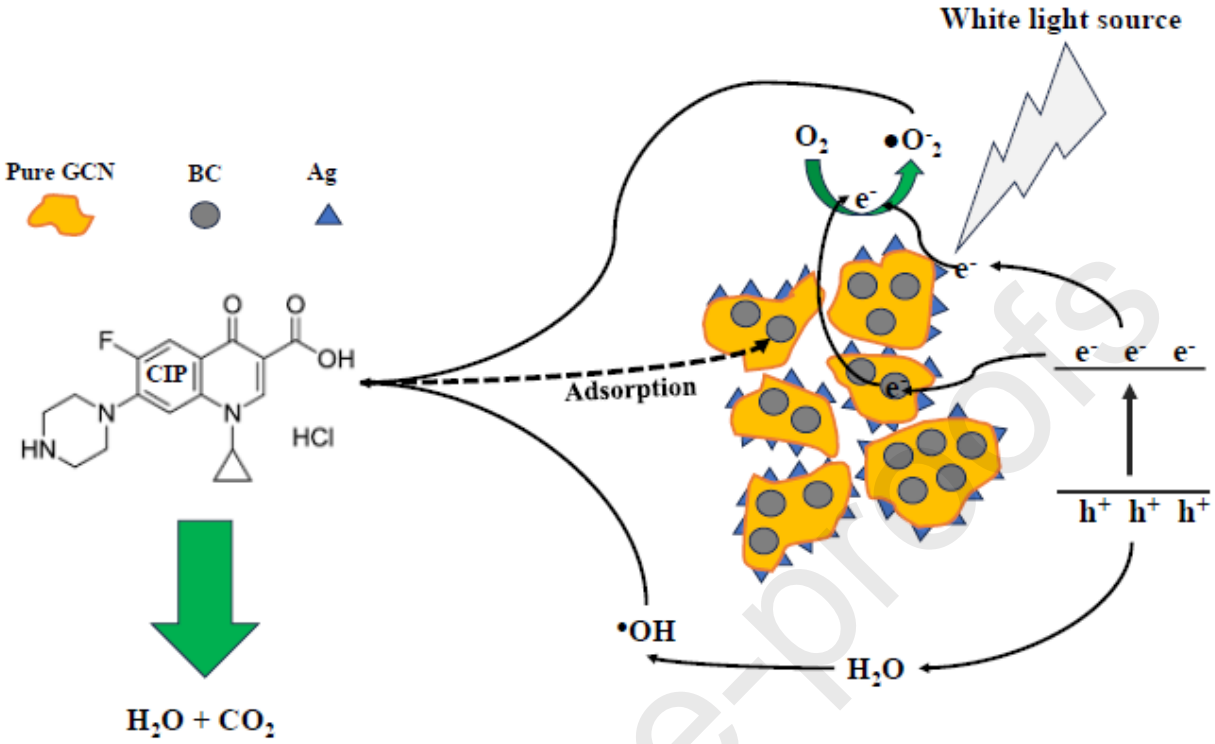

Research highlights

- A ternary material concept is employed for the synthesis of graphitic carbon nitride (GCN) based composite photocatalyst
- Silver (Ag) is employed as dopant for GCN for extended optical absorption
- Biochar is selected as an effective conductive substrate for efficient photogenerated charge separation
- Photocatalytic activity evaluated by degradation of pharmaceutical micropollutant, ciprofloxacin
- Improved photocatalytic performance is ascribed to improved light absorption by Ag dopant and enhanced charge separation due to biochar content

Author Agreement Statement

Title : Silver (Ag) Doped Graphitic Carbon Nitride (g-C3N4)/Biochar composite Photocatalyst for Improved Photocatalytic Degradation of Ciprofloxacin (CIP)

We the undersigned declare that this manuscript is original, has not been published before and is not currently being considered for publication elsewhere.

We confirm that the manuscript has been read and approved by all named authors and that there are no other persons who satisfied the criteria for authorship but are not listed. We further confirm that the order of authors listed in the manuscript has been approved by all of us.

We understand that the Corresponding Author is the sole contact for the Editorial process. He/she is responsible for communicating with the other authors about progress, submissions of revisions and final approval of proofs.

Name and affiliation of all authors:

Ijlal Idrees[1], Muhammad Zafar[2], Malik Adeel Umer[3], Fahad Rehman[1], Abdul Razzaq[1,*], Seongwan Kim[4], Yunsook Yang[4], Woo Young Kim[4,*]

[1] Department of Chemical Engineering, COMSATS University Islamabad, Lahore 54000, Pakistan

[2] Institute of Energy and Environmental Engineering, University of the Punjab, Lahore 54590, Pakistan

[3] School of Chemical and Materials Engineering (SCME), National University of Sciences and Technology (NUST), H-12, Islamabad 44000, Pakistan

[4] Department of Electronic Engineering, Faculty of Applied Energy System, Jeju National University, Jeju-si 63243, Jeju Special Self-Governing Province, Korea

[*] Authors to whom correspondence should be addressed.

Signed by corresponding author instead of all authors as follows:

Prof. Dr. Woo Young Kim